Korean J. Chem. Eng., 36(12), 1971-1982 (2019)
DOI: 10.1007/s11814-019-0407-7

pISSN: 0256-1115
eISSN: 1975-7220

Oxygen transfer capacity of the copper component introduced into the defected-$MgMnAlO_4$ spinel structure in CH_4-CO_2/air redox cycles

Namgyu Son*, Jeong Yeon Do*,†, No-Kuk Park, Ui Sik Kim***, Jeom-In Baek***, Doyeon Lee****, Ho-Jung Ryu****, and Misook Kang*,†**

*Department of Chemistry, College of Science, Yeungnam University, Gyeongsan, Gyeongbuk 38541, Korea
**School of Chemical Engineering, Yeungnam University, Gyeongsan, Gyeongbuk 38541, Korea
***Korea Electric Power Corporation Research Institute, 105 Munji-ro, Yuseong-gu, Daejeon 34056, Korea
****Korea Institute of Energy Research, 152 Gajeong-ro, Yuseong-gu, Daejeon 34129, Korea
(*Received 27 April 2019 • accepted 15 October 2019*)

Abstract−Oxygen carrier particles were fabricated by using defected-$MgMnAlO_4$ as a support particle with crystal defects, and by the Cu^{2+} ions with a higher reduction potential substituted with Mg^{2+} ions, in order to use methane-chemical looping combustion (CH_4-CLC) reaction. The oxygen transfer capacities of the particles were compared when conducting redox reactions under H_2/air or CH_4-CO_2/air systems. As a result, the oxygen transfer capacity increased as the amount of Cu ions added increased. In particular, in the CH_4-CO_2/air system, $Cu_{0.75}Mg_{0.25}MnAlO_4$ particle showed an excellent oxygen transfer capacity of 7.62%. The XPS result confirms that the Cu^{2+} (also partially Mn^{3+} ions) in the $Cu_{0.75}Mg_{0.25}MnAlO_4$ particle oxidize CH_4, and then they are restored to their original state by receiving oxygen from the Al^{3+} and Mg^{2+} ions in the support. The oxygen vacancies in the lattice due to the Cu^{2+} could easily induce oxygen delivery, and the reversible oxygen loss recovery by re-oxidation in the air reactor could be achieved. This is the most important factor in increasing oxygen transfer capacity. Ultimately, in this study, oxygen defects in the crystal lattices induced during the reaction seem to have a positive effect on the CH_4 combustion reaction.

Keywords: Oxygen Carrier, Oxygen Vacancy, Oxygen Transfer Capacity, Methane Combustion

INTRODUCTION

Unlike conventional systems where methane fuel is directly contacted with air or oxygen, methane chemical looping combustion (CH_4-CLC) technology allows oxygen carrier particles to circulate to combust methane indirectly through two reactors (fuel reactors/air reactors) [1]. Therefore, CO_2 can be initially separated without separate collection facilities during the process, and there is no generation of NO_x, which is called the next generation low-pollution technology [2]. At this time, the oxygen carrier particles that transfer oxygen to the methane fuel recover oxygen from the air and then repeat the chemical looping process to be reused. The temperature of the fuel reactor in which the methane combustion takes place and the air reactor in which the oxygen carrier particles are regenerated is about 800 to 1,200 °C; it is possible to generate electricity using the pressure and heat of the gas discharged from the two reactors, and it shows a fairly high efficiency [3]. The most important technology in methane chemical looping combustion is the oxygen transfer capacity of oxygen carrier particles. To date, transition metal oxides including Ni have been mixed with typical metal oxides such as Ca, Mg, and Al [4,5], or multi-complex particles in which divalent transition metals are mixed with Cr, Mn, and Fe transition metals having various oxidation states have been used as the oxygen carriers [6-8]. Based on commercially available materials, the performance of the highest Ni-based oxygen carrier to date has been officially reported to be about 8% [9]. However, this value is still challenging, and oxygen delivery capacity is less than 10% because the transition metal oxides are rapidly degraded due to sintering at high temperatures [10]. Therefore, to prevent sintering of oxygen-transporting metal species at high temperatures, we replaced metal species in stable frameworks in previous studies and prevented them from aggregating at high temperatures [11]. As a result, it was confirmed that the structure was reversibly maintained even in the repeated looping reaction, which meant that it could have a long-time oxygen transfer capability. Furthermore, we confirmed that when the divalent and trivalent transition metals are simultaneously substituted, their synergies increase the oxygen transfer capacity in their redox reaction [12]. It was concluded by oxygen defects, one of the crystal lattice defects caused by metal substitution [13].

But, we did not have an in-depth approach to determine which place in the spinel structure affects crystal defects and, eventually, it could not be identified. Therefore, in this main study, first, it will reveal which metal of A and B sites in the AB_2O_4 spinel structure forms a lattice defect when substituted with another metal. After that, $MgMnAlO_4$ in which Al^{3+} ion sites are replaced with Mn^{3+} ions in $MgAl_2O_4$ as base particles, and Cu^{2+} ions with 0.25, 0.50, and 0.75 moles, which can promote reduction property in redox reaction, are inserted into Mg^{2+} ion site to prepare various oxygen carrier particles. Their oxygen transfer capacities are compared when

†To whom correspondence should be addressed.
E-mail: daengi77@ynu.ac.kr, mskang@ynu.ac.kr

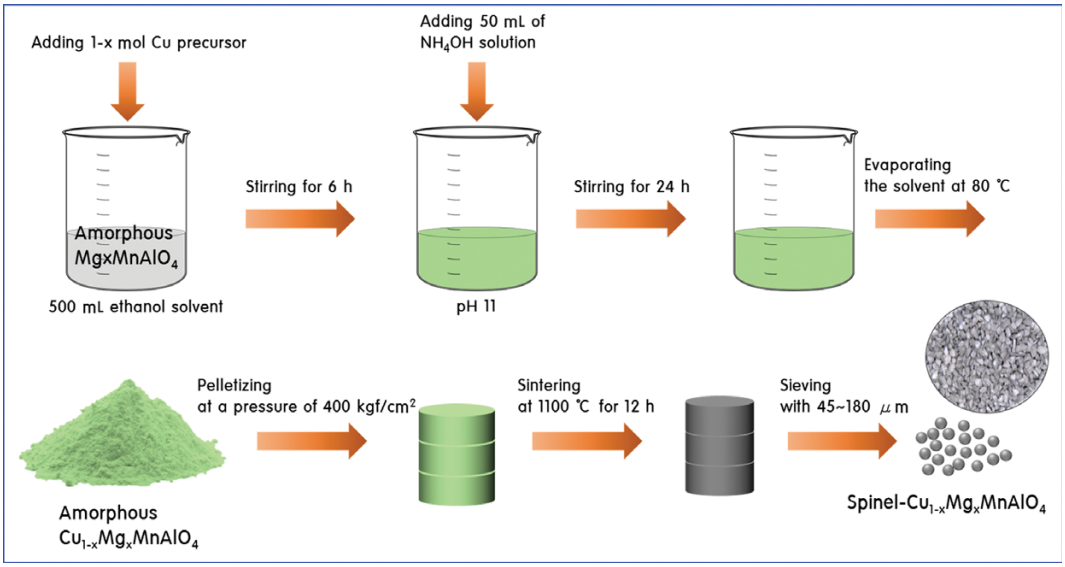

Scheme 1. Preparation process of $Cu_{1-x}Mg_xMnAlO_4$ particles.

the redox reactions occurred under H_2/air or CH_4-CO_2/air conditions. Additionally, the optimum molar content of Cu^{2+} ion with the highest oxygen transfer capacity is discussed.

EXPERIMENTAL

1. Preparation and Characterization of $Cu_{1-x}Mg_xMnAlO_4$ Substituted by Cu Ion into the Defected-$MgMnAlO_4$ Spinel Structure

A distorted-$MgMnAlO_4$ with Mn-substituted $MgAl_2O_4$ framework was first prepared [14]. Using this as a basic substrate, three samples with a $Cu_{1-x}Mg_xMnAlO_4$ spinel structure with 0.25, 0.50, and 0.75 moles of Cu ions substituted by the amount of Mg reduced were synthesized in the order presented in Scheme 1. Amorphous $MgMnAlO_4$ powders were prepared by sol-gel method by quantitatively adding Mg, Mn, and Al starting materials ($MgCl_2{\cdot}nH_2O$, $MnCl_3{\cdot}nH_2O$, and $AlCl_3{\cdot}nH_2O$, 99.95%, Junsei Com, Japan) to distilled water. The powder was put into a 1.0 L beaker containing 500 mL of ethanol and stirred to disperse uniformly. A Cu reagent ($CuCl_2{\cdot}nH_2O$, 99.95%, Junsei Com., Japan) was added to the dispersion solution so that the ratio of Mg : Cu was 0.75 : 0.25, 0.5 : 0.5, and 0.75 : 0.25. Thereafter, the mixture was stirred for 6 h to prepare a uniform colloidal solution. Ammonia water was added to this solution to adjust pH to 11, and then aged for 24 h while stirring again. In the final solution, the ethanol solvent was evaporated at 80 °C to obtain an amorphous $Cu_{1-x}Mg_xMnAlO_4$ powder. The powder was pelletized at a pressure of 400 kgf/cm^2 and sintered at 1,100 °C for 12 h to obtain a spinel $Cu_{1-x}Mg_xMnAlO_4$ powder. In the final step, the pellet was crushed and sieved to collect only particles between 45 and 180 μm and used for the redox cycle reaction. The particles produced in this study were four types of $MgMnAlO_4$, $Cu_{0.25}Mg_{0.75}MnAlO_4$, $Cu_{0.5}Mg_{0.5}MnAlO_4$, and $Cu_{0.75}Mg_{0.25}MnAlO_4$.

2. Characterization of $Cu_{1-x}Mg_xMnAlO_4$ Particles

The crystal structure of the $Cu_{1-x}Mg_xMnAlO_4$ particles, the morphology of the particles, and the composition of the elements constituting the particles were identified by powder X-ray diffraction (XRD, nickel-filtered CuKα radiation, 40.0 kV and 15.0 mA, Miniflex, Rigaku, Japan), Field Emission Scanning Electron Microscope (FE-SEM, 15.0 kV, S-4100, Hitachi, Japan), Field Emission Scanning Transmission Electron Microscope (FE-STEM, 200 kV, Titan G2 ChemiSTEM Cs Probe, FEI Company, USA) and energy dispersive X-ray spectroscopy (EDS, EX-250, Horiba, Japan). The adsorption properties for CH_4 and CO gases on $Cu_{1-x}Mg_xMnAlO_4$ particles were measured by CH_4- and CO-TPD (temperature programmed desorption) experiments using the BELCAT equipment (Bel Japan Inc., Japan). The CH_4 (5.0 vol% CH_4) or CO (5.0 vol% CO) gases were adsorbed, and the titrated temperature range was from 50 to 800 °C at 10 °C min^{-1} under He flow. The desorbed gases were detected using a thermal conductivity detector (TCD) with an online quadrupole mass spectrometer (QMS). To determine the reducing ability and the reduction temperature of the active elements constituting the particles, H_2-temperature programmed reduction (TPR) was conducted with a BELCAT (Bel Japan Inc., Toyonaka, Japan). 0.10 g of the $Cu_{1-x}Mg_xMnAlO_4$ particles were charged into the quartz tube and flushed with high-purity argon gas at 300 °C for 1 h before the TPR measurements, followed by cooling to room temperature. The TPR runs were carried out with a flow of 5 vol% H_2/Ar (ca. 30 mLmin^{-1}) from 50 to 900 °C at a rate of 10 °C min^{-1}. The consumption of H_2 was monitored using a TCD and mass analyzer [Q-mass]. To evaluate the redox mechanism on $Cu_{1-x}Mg_xMnAlO_4$ particles, X-ray photoelectron spectroscopy (XPS, K-Alpha, Thermo Scientific, UK) with a non-monochromatic Al$K\alpha$ (1,486.6 eV) X-ray source was performed before and after the redox cycling, The Cu_{2p}, Mg_{2p}, Mn_{2p}, Al_{2p}, and O_{1s} binding energies in the $Cu_{1-x}Mg_xMnAlO_4$ before and after the redox cycles were determined.

3. Redox Cycling Tests of $Cu_{1-x}Mg_xMnAlO_4$ Particles

To predict the capacity of the oxygen transfer particles of the prepared particles, redox cycling tests were carried out in the similar gas composition in the actual CH_4-CLC reaction as follows. A thermo-

gravimetric analyzer (Shinco co, Korea) was used, and 50 mg of the sample was loaded into an alumina crucible. The TGA was purged with N_2 to introduce an inert atmosphere, and the total flow of 100 mL/min was fixed in all experiments for 10-redox cycles. The crucible was heated to 850 °C for the redox reactions. CH_4 (or H_2) and air gases were used as the reducing and oxidizing gases for the comparison of the performances of the oxygen carrier particles, respectively. A 100 mL/min flow of 15% CH_4 (or H_2) balanced with CO_2 (or N_2) was first introduced into the TGA apparatus. The weight loss of particles was recorded as a function of time. Following the reduction reaction, a 100 mL/min flow of 100% air was fed into the TGA apparatus. During each redox cycle, the samples were kept for 900 s in a reducing atmosphere and 600 s in an oxidizing atmosphere with a short inert period of 150 s in between. The fixed residence time and gas composition were set similar to the actual operating conditions of the circulating fluid bed CLC process [15].

RESULTS AND DISCUSSION

1. Characteristics of $Cu_{1-x}Mg_xMnAlO_4$ Particles

Before going into the actual work of this study, we compared the physical properties of $MgAl_2O_4$ and $MgMnAlO_4$ particles as shown in Fig. 1. To accurately identify the defect sites in $MgAl_2O_4$ crystals, $MgMnAlO_4$ substituted Al^{3+} ions with Mn^{3+} and $Mg_{0.5}Cu_{0.5}Al_2O_4$ substituted Mg^{2+} with Cu^{2+} ions were synthesized, and their structures were confirmed. As a result, the 2-theta positions of XRD peaks did not change even when the bivalent transition metal (ex. Cu^{2+}) ion with large size was substituted for A^{2+} ion site having six-coordination in AB_2O_4 type as shown in Fig. 1(a). However, when the B^{3+} ion site with four-coordination was substituted with a large trivalent transition metal (ex. Mn^{3+}) ion, the 2-theta positions of the XRD peaks shifted to the lower angles. This implies that the Al-O lattice distance was increased by the Mn^{3+}-substitution in the tetrahedral structure, which is a proof that crystal defects such as oxygen and metal defects were formed in the tetrahedral metal-O site [16]. On the other hand, we did not expect a redox reaction in $MgAl_2O_4$, since there was no reduction peak for pure $MgAl_2O_4$ in the H_2-TPR results as shown in Fig. 1(b). However, by replacing the Mn^{3+} ion into the Al^{3+} ion site, it was confirmed that Mn^{3+} to $Mn^{2.5+}$ or Mn^{2+} was reduced at 600 °C, which means that the redox reaction can occur at high temperatures. After the powdered particles are pelletized and crushed to 45-180 μm, their surface appears to increase porosity as Mg is displaced as shown in Fig. 1(c). In addition, the amount of Mn^{3+} ions actually incorporated into the framework was doubled as to 2 : 1, not 1 : 1 relative to the amount of Al^{3+} ions, which implies that the Mn^{3+} ion was replaced by a fairly stable substitution in the framework of $MgAl_2O_4$ as shown in the EDS results (Fig. 1(d)). When the surface charges are calculated based on the EDS data, the charges of the metal cations are all about 100, and the anion charge generated from the oxygen is about 120, which contained more oxygen in the lattice. This is expected to be due to the Frankel defects resulting from the cations escaping from the lattice (eventually increasing the lattice oxygen). These defects can increase the active sites of oxygen carrier particles, which in turn can improve oxygen transfer capacity [17].

As a result, it was confirmed that lattice defect is generated when the B metal of the spinel structure AB_2O_4 is replaced with another metal. As an essential step, Cu^{2+} ions, which are active metals, were substituted for defective spinel $MgMnAlO_4$ particles at a molar ratio instead of Mg^{2+}, and XRD patterns of the obtained $Cu_{1-x}Mg_xMnAlO_4$ particles are shown in Fig. 2. The crystal structure of $MgMnAlO_4$, which is the base material in this study, is perfectly matched to the spinel structure of $MgAl_2O_4$, which is a starting material composed of tetrahedral MgO and Al_2O_3 octahedral [18]. When the $MgMnAlO_4$

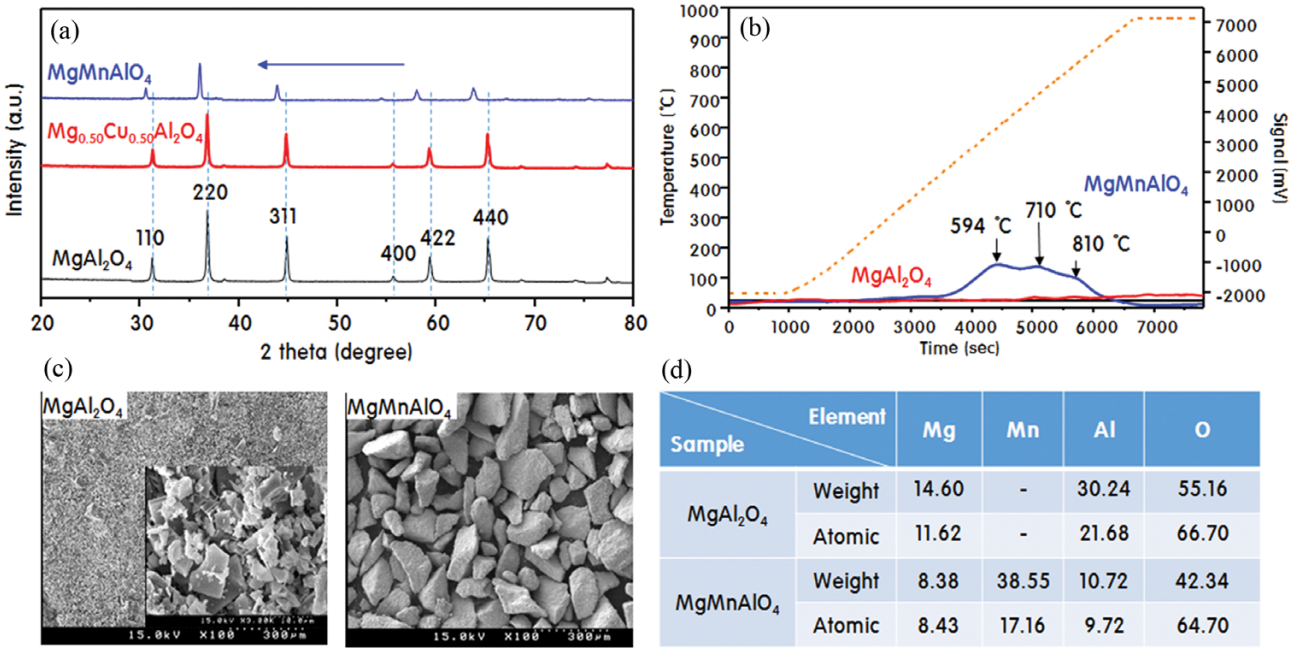

Sample	Element	Mg	Mn	Al	O
$MgAl_2O_4$	Weight	14.60	-	30.24	55.16
	Atomic	11.62	-	21.68	66.70
$MgMnAlO_4$	Weight	8.38	38.55	10.72	42.34
	Atomic	8.43	17.16	9.72	64.70

Fig. 1. The XRD patterns (a) H_2-TPR (b) SEM images (c) and EDX atomic ratio analysis table (d) of $MgAl_2O_4$ and $MgMnAlO_4$.

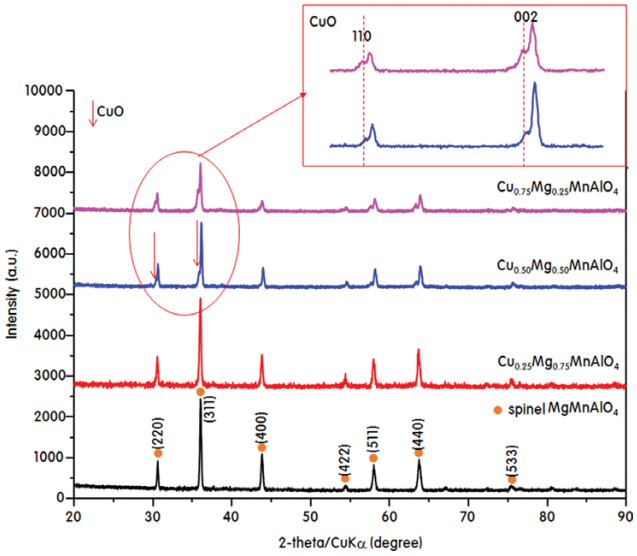

Fig. 2. X-ray diffraction patterns of $Cu_{1-x}Mg_xMnAlO_4$ particles.

framework was substituted with 0.25 mol Cu ions instead of Mg, the 220 and 311 crystal planes of the spinel structure were slightly broadened and the peak intensity was small, but the peak corresponding to CuO was not observed. However, when the Cu content was increased to 0.5 mol, the shoulder peaks corresponding to the 110 and 002 planes of the monoclinic CuO (2-theta=32.41 and 35.59°, base-centered C2c space group) were shown [19]. The intensity of this peak was larger when 0.75 moles of Cu ions were substituted. From this result it can be expected that Cu was substituted in the A (Mg) site with the tetrahedral coordination of the cubic lattice (a=b=c, $\alpha=\beta=\gamma$) in the AB_2O_4 spinel structure [20], that the distance of an axis of Cu-O became long and eventually the orthorhombic lattice changed into a distorted monoclinic lattice form.

Fig. 3 displays the HRTEM (High-resolution transmission electron microscopy) images, SAED (Selected area electron diffraction) pattern and lattice spacing images of $Cu_{0.75}Mg_{0.25}MnAlO_4$ sample with higher Cu content. HRTEM images clearly shows the sheet-like structure for $Cu_{0.75}Mg_{0.25}MnAlO_4$ sample and SAED pattern shows the corresponding lattice spacing in different crystalline plane directions. Although the shape appears amorphous, in the SAED pattern, a continuous ring corresponding to each diffraction peak observed in the XRD was identified. The lattice distances of 111, 220, 311, and 400 crystal planes of $Cu_{0.75}Mg_{0.25}MnAlO_4$ particles were 4.52, 2.94, 2.48, and 2.05 Å, respectively. On the other hand, the lattice distances of (220) and (311) planes were calculated as 2.92 and 2.44 Å, respectively, for pure $MgMnAlO_4$ sample. The observed changes in lattice distances are due to the doping of Cu into

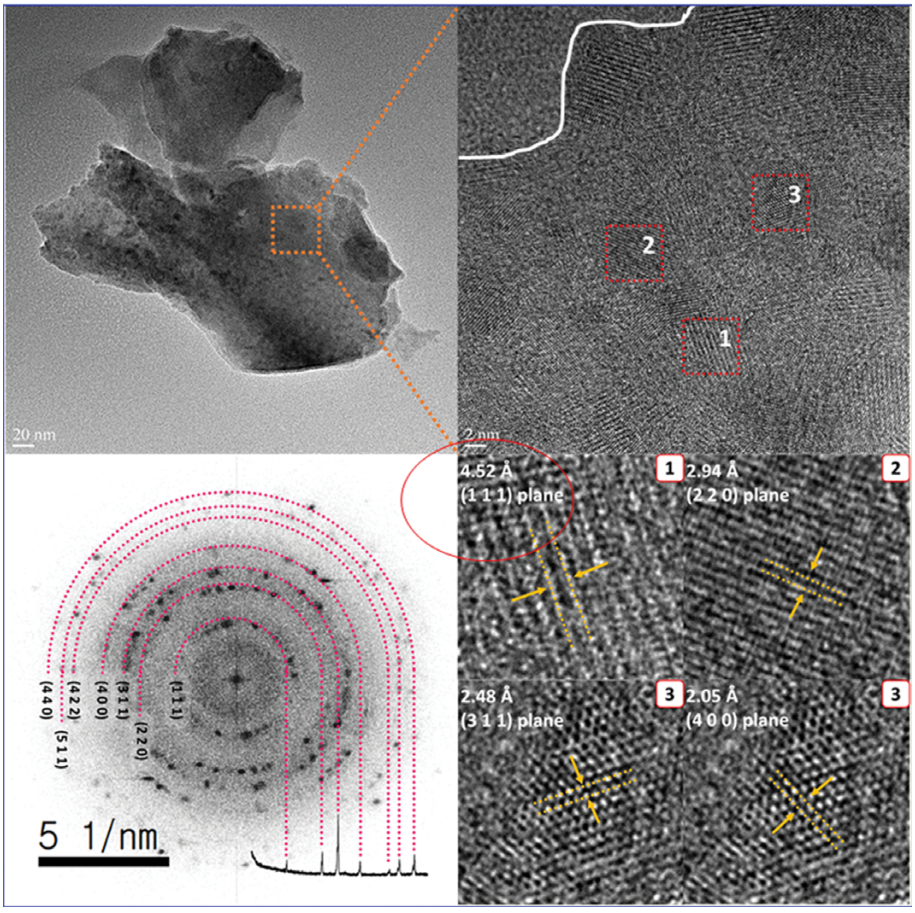

Fig. 3. HR-TEM image and electron diffraction pattern of $Cu_{0.75}Mg_{0.25}MnAlO_4$ particles.

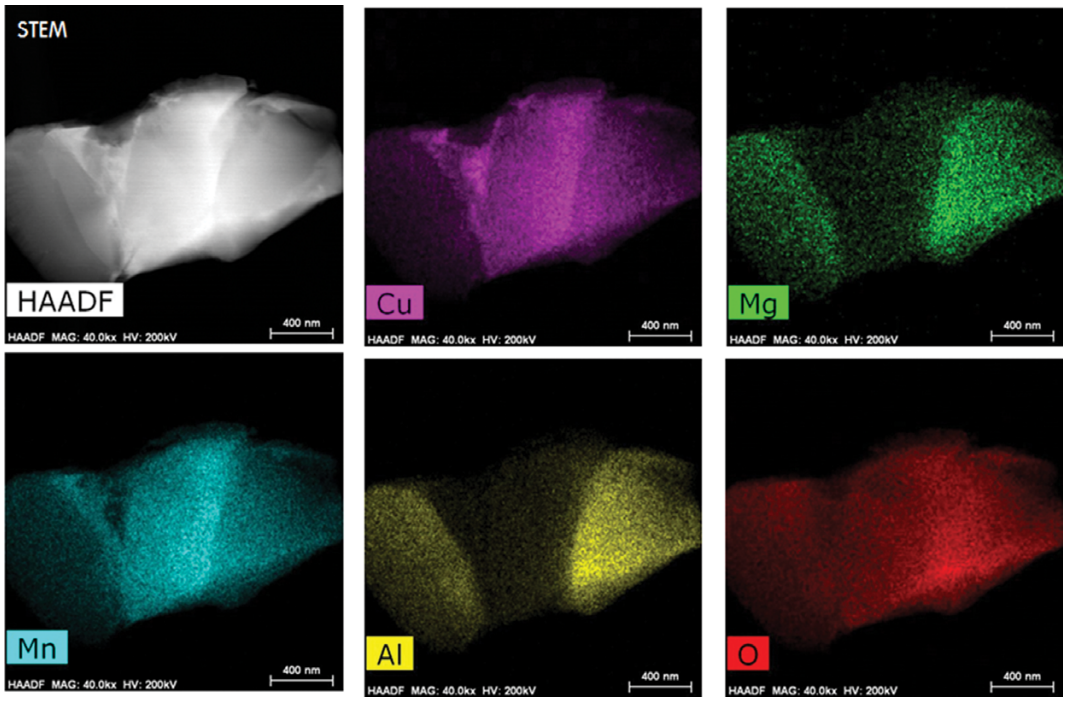

Fig. 4. FE-STEM image and EDS mapping images of $Cu_{0.75}Mg_{0.25}MnAlO_4$ particles.

$MgMnAlO_4$ structure, which is consistent with the XRD results.

Fig. 4 shows STEM image and element mapping images of $Cu_{0.75}Mg_{0.25}MnAlO_4$. It was observed that all of the elements were uniformly distributed throughout the particle, and the intensity of the color of the elements matched the concentration of the additive. The O, Mn, and Cu components were much more colored, followed by Al and Mg, respectively. When we compared the distribution of colors by integrating the components dispersed throughout the particle from HAADF (High-Angle Annular Dark-Field), the Cu and Mn components were concentrated in the center. It is expected from this result that in the cubic spinel structure, Cu and Mn ions are well substituted in the tetrahedral (Mg) and octahedral (Al) sites, respectively.

EDS was measured to quantitatively determine the content of the components present in the particles, and the results are shown in Table 1. The atomic amount of substituted actual Cu instead of Mg was 3.92, 8.43, and 12.42 for $Cu_{0.25}Mg_{0.75}MnAlO_4$, $Cu_{0.5}Mg_{0.5}MnAlO_4$, and $Cu_{0.75}Mg_{0.25}MnAlO_4$, respectively. It can be seen that it is close to the stoichiometric value as compared with the amount of the starting material added in the synthesis process. In addition, the amount of Mg was relatively decreased with the increase of Cu amount, and this result indirectly shows that most of Cu is substituted by Mg. On the other hand, the amount of Mn was not significantly changed by the change of the amount of Cu and Mg, whereas the amount of Al was increased in Cu 0.25 mol substituted particles, but there was no change thereafter. In the $MgMnAlO_4$ particles, the ratio of Mg to Al was nearly 1 : 1 with Mn substitution, and the amount of Cu and Mg combined with 0.25 moles of Cu was almost the same as that of Al. However, in the case of 0.5 moles of Cu added, the amount of Mg combined with Cu increased to 1.5-times as much as the amount of Al. From this result, it can be seen that when Mn was added and stabilized in the $MgAlO_4$ crystal, no movement occurred when any other metals were substituted, and rather, Al present in the support from the

Table 1. Elemental abundance ratios of $Cu_{1-x}Mg_xMnAlO_4$ particles determined by EDS

Sample \ Element		Cu	Mg	Mn	Al	O
$MgMnAlO_4$	Weight (%)	-	8.38	38.55	10.72	42.34
	Atomic (%)	-	8.43	17.16	9.72	64.70
$Cu_{0.25}Mg_{0.75}MnAlO_4$	Weight (%)	9.61	9.14	32.15	12.66	36.44
	Atomic (%)	3.92	9.74	15.16	12.16	59.02
$Cu_{0.50}Mg_{0.50}MnAlO_4$	Weight (%)	19.17	4.14	33.22	8.46	35.01
	Atomic (%)	8.43	4.76	16.90	8.76	61.15
$Cu_{0.75}Mg_{0.25}MnAlO_4$	Weight (%)	27.07	1.95	29.12	8.75	33.11
	Atomic (%)	12.42	2.34	15.45	9.45	60.33

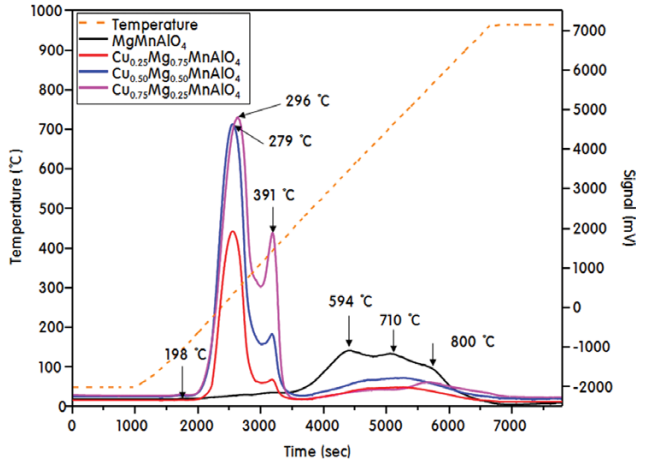

Fig. 5. H_2-TPR curves of $Cu_{1-x}Mg_xMnAlO_4$ particles.

beginning was closely related to the addition of the divalent metal. This indicates that the transition metal is more stable than the typical metal in the spinel structure with four or six coordination positions.

2. Gas Adsorption/Desorption Behavior on $Cu_{1-x}Mg_xMnAlO_4$ Particles

The performance of CLC depends on the oxygen transfer capacity of the particles, which is directly influenced by the reduction of the oxygen carrier particles and the reduction temperatures [21]. Therefore, the H_2-TPR experiment was performed, and Fig. 5 shows the result. Generally, in the H_2-TPR results, the curved region corresponds to hydrogen uptake, and the curved position indicates how much and how easily the active metal species is reduced [22]. In the $MgMnAlO_4$ particles, curves corresponding to $Mn^{3+}\rightarrow Mn^{2+}$ were observed near 594, 710, and 800 °C [23]. Qiu et al. [24] reported that the H_2-TPR curves are different when the Mn oxide is loaded alone into the support and sintered with other metals. In the latter case, the H_2-TPR curve was shifted to higher temperatures and separated into more reduction curves. In addition, Huo et al. reported [25] that the Al-connected CuO has higher thermal stability than CuO. The metal elements incorporated into the lattice of the structure were reduced at higher temperatures. Based on these results, the three curves shown in our study are attributable to the following: Mn^{3+} ions are substituted on the Al^{3+} site of the $MgAl_2O_4$ structure and are stable to the spinel framework and are therefore difficult to reduce. Therefore, Mn^{3+} ions substituted in the skeleton were reduced to Mn^{2+} at a high temperature of 710 or 800 °C, and Mn^{3+} ions that were not substituted on the framework and remained on the surface were expected to be reduced to Mn^{2+} at a low temperature of 594 °C. This means that the CLC reaction must be performed above 850 °C for $MgMnAlO_4$ particles to use all of the redox capabilities of Mn. In Cu-added samples, gradual reduction curves of $Cu^{2+}\rightarrow Cu^0$ and $Cu^{+}\rightarrow Cu^0$ are observed near 276-296 °C and 391 °C [25]. As the amount of Cu increases, the intensity of the curve increases, and the curve shifts slightly to the high temperature. In addition, as the Cu content increases, the Mn^{3+} reduction curves are also slightly shifted to higher temperatures, but the amount is much smaller. From the results of Cu reduction at a fairly low temperature, actual methane CLC is expected to be possible at temperatures lower than 500 °C. However, to understand the synergistic effect of Cu and Mn, we recognized that CLC and redox reaction should be performed at 850 °C or higher.

Generally, the CLC reactivity is also increased when the CH_4 fuel adsorption on the oxygen carrier surface in the CLC reaction increases [26]. In addition, the ultimate goal of the CLC reaction is to completely oxidize CH_4 to CO_2. At this time, CO is generated as an intermediate, which is again converted into carbon dioxide by the oxygen of the oxygen carrier. Therefore, adsorption experiments on CH_4 and CO in oxygen carriers are very important, and Fig. 6(a) and (b) show CH_4- and CO-TPD curves for $Cu_{1-x}Mg_xMnAlO_4$ particles. In the $MgMnAlO_4$ particles, CH_4 desorption was observed with one broad curve near 960 °C. This means that methane is strongly adsorbed on the surface of $MgMnAlO_4$ particles, and binds to the oxygen of the particles to desorb as mainly CO or CO_2. On the other hand, desorption of CH_4 was observed in two places with Cu addition, and in particular, a sharp curve was observed around 810 °C, and the strength of the curve was strengthened in proportion to the amount of Cu. Furthermore, when the curve sizes at 810 and 960 °C were compared, the methane desorption curve at 810 °C increased as the Cu content increased, and the CH_4 desorption curve at 960 °C increased as the Cu content decreased. We

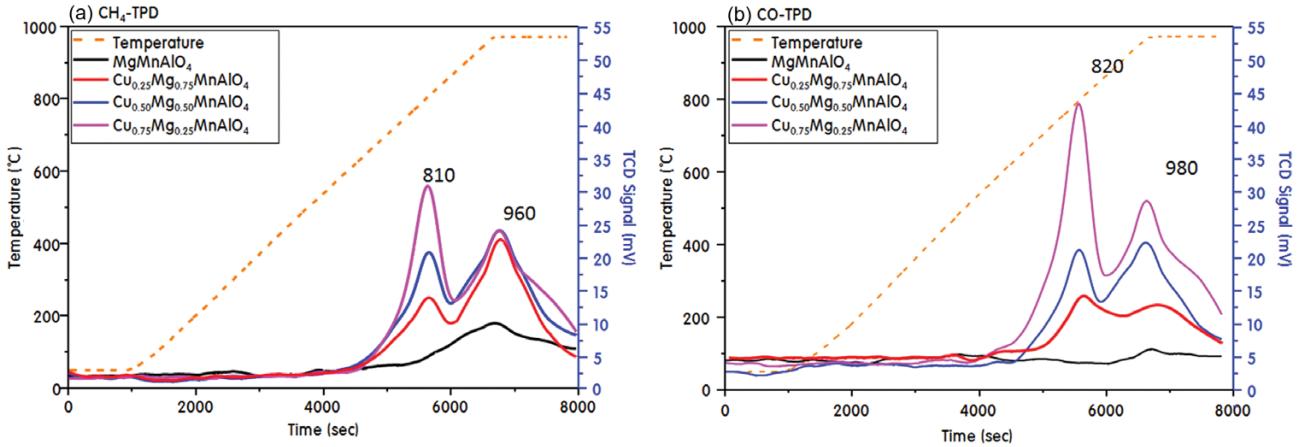

Fig. 6. CH_4- (a) and CO- (b) TPD curves of $Cu_{1-x}Mg_xMnAlO_4$ particles.

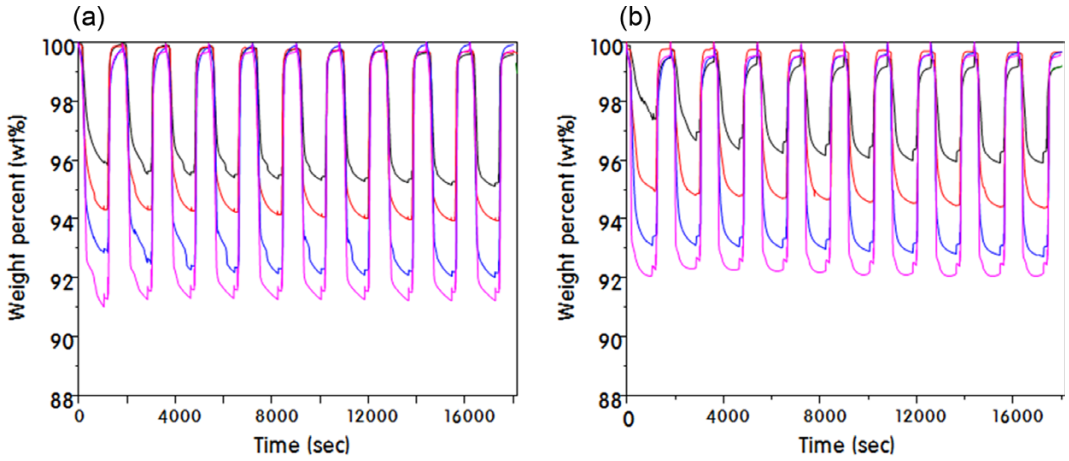

		$MgMnAlO_4$	$Cu_{0.25}Mg_{0.75}MnAlO_x$	$Cu_{0.50}Mg_{0.50}MnAlO_x$	$Cu_{0.75}Mg_{0.25}MnAlO_x$
Roc,t (wt%)	H_2-N_2/air	4.474	6.139	7.870	8.327
	CH_4-CO_2/air	3.531	5.312	7.123	7.615

Fig. 7. Redox cycles in the H_2-N_2/air (a) and CH_4-CO_2/air (b) redox systems of $Cu_{1-x}Mg_xMnAlO_4$.

have already reported the following results in previous study [27]: The desorbed C_3H_8 molecules from the metal oxides showed three desorption curves at 500, 750, and 850 °C and the mass spectra signals were exhibited at m/z=16(CH_4), 43(CH_3CHO), and 28(CO). Therefore, in this study, desorption curves at 810 and 960 °C in CH_4-TPD are probably considered to be CO in which CH_4 partially reacts with the oxygen of the metal oxide. Qian et al. also reported [28] that the CH_4-TPD process actually involving the surface residual oxygen species on catalysts. CO and CO_2 produced during the TPD process might originate from partially reduced residual oxygen bonded to metal. In conclusion, it was confirmed that Cu ion adsorbs CH_4 relatively more than Mn ion and desorbs at lower temperature. Applying these particles to actual CLC reactions, it is believed that CLC performance is also improved and coke deposition associated with particle degradation is inhibited. On the other hand, the shape of the CO desorption curve in Fig. 6(b) is similar to the CH_4 desorption curve. It was found that CO-TPD established that two kinds of CO adsorption states exist on the catalyst and are desorbed in the form of CO_2 at different temperatures by the CO disproportionation reaction [28]. Here, adsorbed CO molecules maybe combine with oxygen in the oxygen carrier at high temperatures to desorb CO_2 [29]. CO_2 desorption was hardly observed in $MgMnAlO_4$ particles. This means that using $MgMnAlO_4$ particles methane will not be completely burned to CO_2 but will remain as CO. In the particles with 25% Cu substitution, one desorption peak was observed at around 980 °C and two desorption curves were observed at 820 and 980 °C for Cu substituted particles of 50% or more. Furthermore, the intensity and area of these two peaks increased with increasing Cu content. From this result, it can be expected that the oxidation of CO is promoted on Cu ions, and the complete oxidation of CH_4 occurs. We have already suggested in previous studies that Cu does not adsorb CO_2 [30]. However, in those studies, Cu was coexisting with Fe oxide, and Fe ions were more strongly interacting with CO, so that CO was not adsorbed to Cu relatively. However, in this study, it is considered that Mn did not strengthen interaction with CO more than Fe. Therefore, CO is adsorbed onto Cu oxide rather than Mn, and consequently, both CH_4 and CO are considered to take oxygen from Cu oxide and convert to CO or CO_2.

3. Redox Cycle Tests on $Cu_{1-x}Mg_xMnAlO_4$ Particles

To estimate the oxygen transfer capacity of the $Cu_{1-x}Mg_xMnAlO_4$ particles in the CLC reaction, oxidation-reduction circulation experiments were performed in H_2-N_2/air and CH_4-CO_2/air redox systems. All the particles were pulverized and sieved, and only particles with a size of 45 to 180 μm were used; the reaction temperature was fixed at 850 °C. A cycle repeat experiment was carried out over a total of ten times, and the results are shown in Fig. 7. The curves represent the amount of oxygen reduced in the particles as the particles are reduced, which means the amount of oxygen transfer. At this time, the weight decreasing line corresponds to the reduction and the weight increasing line corresponds to the oxidation. In general, when oxidation-reduction occurs quickly and stably, the lines are close to a straight line, which is responsible for the redox rate. The oxygen transfer capacities of the $MgMnAlO_4$ particles after ten cycles were 4.47% and 3.53% in the H_2-N_2/air and CH_4-CO_2/air redox systems, respectively, suggesting that Mn^{3+} also participates in the redox reaction do. On the other hand, in the $Cu_{0.25}Mg_{0.75}MnAlO_4$ particle substituted with Cu 25%, the oxygen transfer capacities were 5.74% and 5.31% in the H_2-N_2/air and CH_4-CO_2/air redox system, respectively. These were 16% and 21% more than $MgMnAlO_4$ particles. This result implies that Cu substitution has a greater effect on the CH_4-CO_2/air redox system. Furthermore, the oxygen transfer capacity increased proportionally with the amount of Cu. The oxygen transfer differences between CH_4-CO_2/air and H_2-N_2/air systems in the $MgMnAlO_4$, $Cu_{0.25}Mg_{0.75}MnAlO_4$, $Cu_{0.5}Mg_{0.5}MnAlO_4$, and $Cu_{0.75}Mg_{0.25}MnAlO_4$ particles were 0.94, 0.83, 0.75, and 0.71%,

respectively. Thus, the differences in capacity between the two systems decreased as the amount of Cu increased. This result shows that the greater amount of Cu substituted because of the fixed amount of Mn, the more favorable the oxidation occurs because of the adsorption of CH_4 on Cu. As the cycle in the CH_4-CO_2/air redox system increased in the $Cu_{0.75}Mg_{0.25}MnAlO_4$ particle with 75% Cu replaced, the curve patterns became dull. The performance difference between $Cu_{0.5}Mg_{0.5}MnAlO_4$ and $Cu_{0.75}Mg_{0.25}MnAlO_4$ particles was not greater. There is a limit to the concentration of Cu that can be substituted in the spinel framework. Thus, as already mentioned in the XRD results, most of the 0.75 mol Cu ions are substituted into the spinel framework, but some are not substituted and remain on the particle surface. The strong sintering due to the entanglement between the remaining copper particles at high temperatures could eventually lead to the Cu-substituted spinel structure. The oxygen transfer capacity in $Cu_{0.75}Mg_{0.25}MnAlO_4$ particle was 7.615% after ten cycles. Adánez et al. already compared the oxygen transfer capacities in several single transition metals according to their weight content [31]. In their work, the oxygen carrier reactivity corresponding to the 5-cycle was used for comparison purposes. Reactivity data were obtained in TGA tests from the weight variations during the reduction and oxidation cycles as a function of time at 950 °C. They showed the transfer capacity of the oxygen carriers corrected by the active metal oxide content in which the capacity of the carrier obviously decreases due to the presence of the inert. In their paper, the oxygen transfer capacity of the Cu oxide oxygen carrier with a Cu content of 40% was 8.04%. Converting this value to 25% of the amount of Cu in the $Cu_{0.75}Mg_{0.25}MnAlO_4$ particle is equivalent to 5%, which is about 2.615% lower than the oxygen transfer capacity of 7.615% of $Cu_{0.75}Mg_{0.25}MnAlO_4$. This result is attributed to the fact that the Cu components added from the $Cu_{0.75}Mg_{0.25}MnAlO_4$ particle were stably inserted in the spinel structure, and their crystal phases did not change after repeated redox reactions. Furthermore, a synergism of Mn^{3+} is considered to be involved here. Calculating and comparing theoretical oxygen transfer capacities makes it easy to judge. The theoretical oxygen transfer capacity is the weight of oxygen that can be delivered by 1.0 g of oxygen carrier, and the metal oxides contained in each particle are consumed the amount of oxygen. Thus, expressed in one equation, theoretical oxygen transfer capacity=[g-O_2/g-particle]. If all the metals in the $Cu_{0.75}Mg_{0.25}MnAlO_4$ particle participate in oxygen transfer, the capacity is calculated as 14%. If only the copper oxide in the particle contributes as an oxygen carrier, the theoretical oxygen transfer capacity is about 3.5%, since it is the amount of oxygen corresponding to $Cu_{0.75}O_{0.75}$. However, the experimental values obtained from these experiments exceeded 3.5%, presumably the active metals acting as oxygen carriers in this study are Cu and Mn. Thus, recalculating the oxygen bound to these two metals, i.e., corresponding $Cu_{0.75}O_{0.75}$ and MnO, the theoretical capacity is 8.2%. The difference between the theoretical oxygen transfer capac-

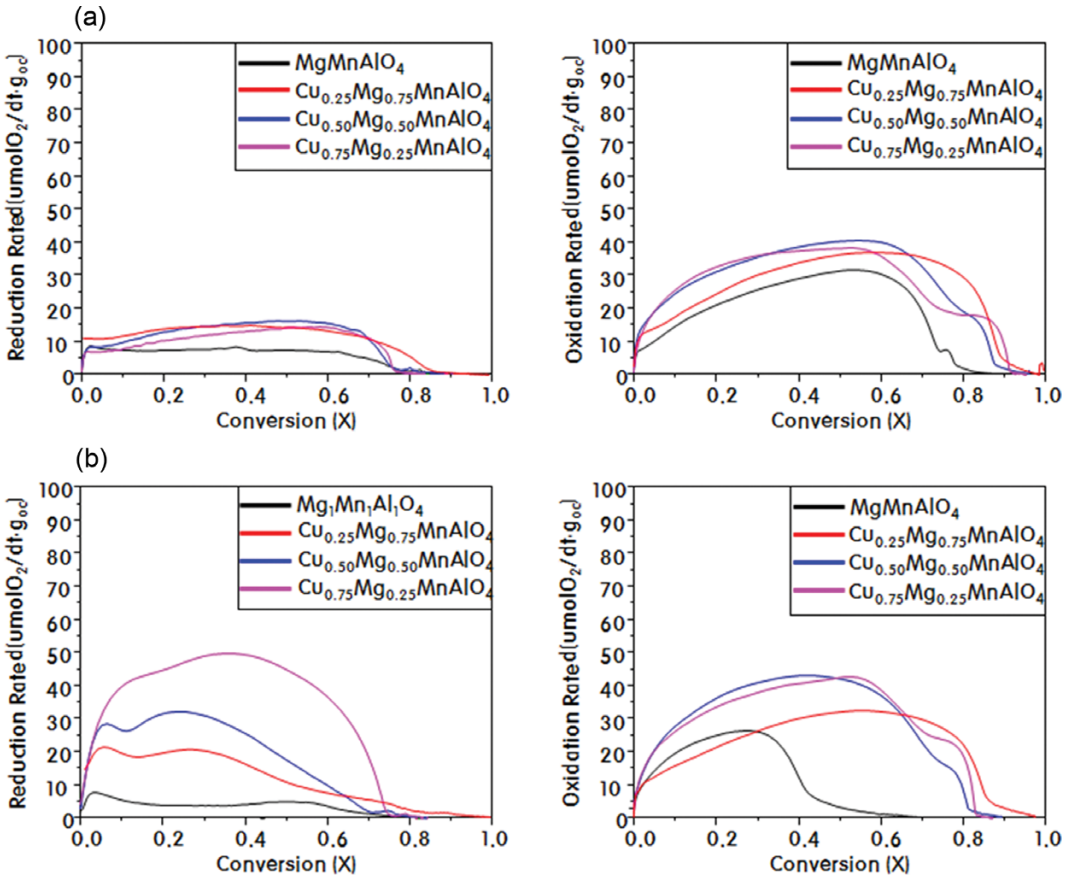

Fig. 8. Conversion ratios versus kinetic rates in the H_2-N_2/air (a) and CH_4-CO_2/air (b) redox systems for $Cu_{1-x}Mg_xMnAlO_4$.

ity and the experimental value (about 0.58%) is thought to be attributed to the fact that the redox reaction was carried out at a low temperature of 850 °C, and all of the Mn components were not involved in the redox reaction.

Fig. 8(a) and (b) compare the reduction conversion (or oxidation conversion) for the reduction rate (or oxidation rate) in H_2-N_2/air and CH_4-CO_2/air redox systems for $Cu_{1-x}Mg_xMnAlO_4$ particles. The oxidation and reduction conversion ratios of the particles were obtained from the following equation [32].

$$\text{Reduction conversion rate: } X_{red}=[m_{ox}-m]/[m_{ox}-m_{red}] \quad (1)$$

$$\text{Oxidation conversion rate: } X_{ox}=1-[m_{ox}-m]/[m_{ox}-m_{red}] \quad (2)$$

In the H_2-N_2/air system of Fig. 8(a), the oxidation rate in all the particles was much faster than the reduction rate, and the difference was about three times. What is remarkable is that in the results of Fig. 7, the oxygen delivery capacity increased with increasing Cu content, but this figure was slightly different. The reduction and oxidation rates of $Cu_{0.5}Mg_{0.5}MnAlO_4$ particles were higher than $Cu_{0.75}Mg_{0.25}MnAlO_4$ particles. On the other hand, in the CH_4-CO_2/air system, as the amount of Cu substitution increased, the reduction rate greatly increased. This result implies that the reduction rate ultimately depends on the amount of Cu ions. Also, the reduction rate of $Cu_{0.75}Mg_{0.25}MnAlO_4$ particles was faster than the oxidation rate. This means that the Cu component in the $Cu_{0.75}Mg_{0.25}MnAlO_4$ particles converted from CuO to Cu as the reaction progressed, suggesting that CO poisoning can occur. On the basis of this result, the reduction rate showed the highest value in the $Cu_{0.75}Mg_{0.25}MnAlO_4$ particles and the oxidation rate was the highest in the $Cu_{0.5}Mg_{0.5}MnAlO_4$ particles, so that the optimum amount of Cu substitution is between 0.5 and 0.75 mol.

4. Characteristics on $Cu_{1-x}Mg_xMnAlO_4$ Particles after CH_4-CO_2/Air Redox Cycle Tests

We have investigated the changes in metal oxide redox state and the crystal structure present in the reaction of the before/after particle. The $Cu_{0.75}Mg_{0.25}MnAlO_4$ particle, which exhibited the highest oxygen delivery capacity, was treated under three conditions: particle before the reaction (a, fresh particle), particle treated for 1 h with a CH_4/CO_2 mixed gas after a 10th redox cycle reaction (b, reduced particle), and particle treated with b for 1 h in an air atmosphere (c, re-oxidized particle). Their XRD patterns are compared in

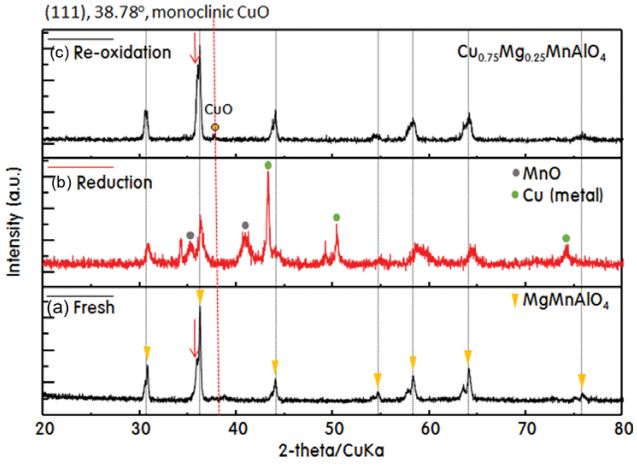

Fig. 9. XRD patterns of fresh $Cu_{0.75}Mg_{0.25}MnAlO_4$, the oxidized by air, and the reduced by CH_4/CO_2 gas.

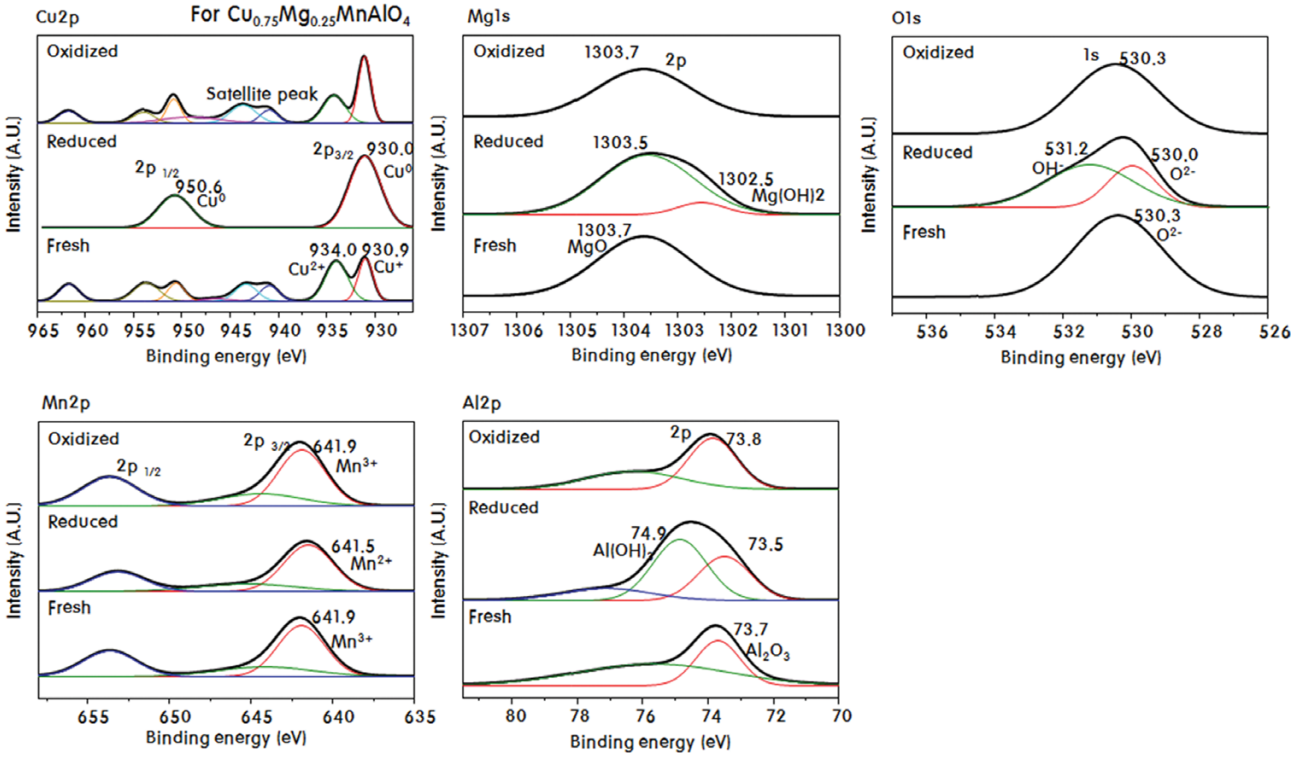

Fig. 10. XPS patterns of Cu_{2p}, Mn_{2p}, Mg_{1s}, Al_{2p}, and O_{1s} of $Cu_{0.75}Mg_{0.25}MnAlO_4$ particle in the fresh state, after reduction, and after oxidation.

Fig. 9. The XRD diffraction pattern of the fresh particle was similar to the spinel structure of $MgMnAlO_4$, and reduced metallic Cu crystals [33] and MnO crystal [34] peaks were observed in the reduced particle after the reaction. However, the complete spinel structure reappears in the re-oxidized particle, and the peaks are slightly broadened, which means that the particle size is reduced [35]. The diffraction peak corresponding to the (111) crystal face of the monoclinic CuO was observed at 2-theta=38.78°. It is deemed that all of the Cu added during the synthesis is not completely anchored in the spinel structure but is also partially present outside the particle surface. As a result, it means that the optimum amount of Cu substitution that can be inserted into the lattice is smaller than 0.75 mol. However, the amount of isolated was not so much. Moreover, we could foresee that Cu substitution partially reduced the oxygen in the spinel lattice, leading to oxygen deficiency and then recovered. In general, oxygen defects in the lattice are known to increase the adsorption of reactive gases and increase the rate of oxygen delivery, positively affecting the combustion reaction [36].

The oxidation state of the metals before and after the redox reaction was compared to check whether the lattice oxygen defects actually occurred during the redox process. Fig. 10 shows the XPS spectra of Cu_{2p}, Mg_{2p}, Mn_{2p}, Al_{2p}, and O_{1s} peaks, which are the main metals in the $Cu_{0.75}Mg_{0.25}MnAlO_4$ particle. The samples were the same as those used in the XRD analysis of Fig. 9. XPS curves corresponding to the Cu2p3/2 spin-orbital in the fresh particle were attributed to CuO and Cu_2O [37], which were located at bond energies of 934.0 and 930.9 eV, respectively. In the reduced sample, however, one large curve appeared at 930.0 eV, which is the binding energy corresponding to metallic Cu [38]. In the re-oxidized sample, the curve of Cu_2O was stronger than that of the fresh particles (well matched with the XRD results already mentioned in Fig. 9), but the corresponding binding energy locations did not change significantly compared to the fresh particle. This result suggests that the oxidation state of Cu in the redox reaction is changing as $Cu^{2+}/Cu^{+}(>1)\rightarrow Cu^{0}\rightarrow Cu^{2+}/Cu^{+}(<1)$. The Mg1s binding energy corresponding to MgO is located at 1,303.5-1,303.7 eV [39]. In the reduced sample, a small curve corresponding to Mg-OH [40] was observed at 1,302.5 eV. However, since the binding energy position or area for MgO was hardly changed in the three samples, Mg did not affect the redox reaction. On the other hand, the Mn2p3/2 binding energy position in the fresh sample was shown at 641.9 eV, which means Mn^{3+}, and in the reduced sample at 641.5 eV, which means Mn^{2+}, and again in the re-oxidized sample at 641.9 eV [39]. In particular, the curve area in the re-oxidized sample was significantly increased. This result implies that Mn^{3+} affects the reaction by changing the oxidation state from $Mn^{3+}\rightarrow Mn^{2+}\rightarrow Mn^{3+}$ in the redox reaction (actually CH_4-CLC) [41]. On the other hand, $Al_{2p3/2}$ binding energy curves attributed to Al^{3+} in the fresh, the reduced, and the re-oxidized samples were 73.7, 73.5, and 73.7 eV, respectively. In particular, in the reduced sample this curve was very large. In addition, the binding energy corresponding to Al-OH was observed in all samples at 74.9 eV, but this peak was reduced in the reduced sample. In general, the observation of M-OH curves implies that M-O in the lattice is broken during the reduction reaction, resulting in oxygen defects [42]. In this study, we have observed that oxygen vacancies are formed in the lattice during the reduction reaction of $Cu_{0.75}Mg_{0.25}MnAlO_4$ particle, and the sites are restored when they are oxidized again. Based on these results, we could guess the role of metals in the particles. First, CH_4 molecules are adsorbed on the

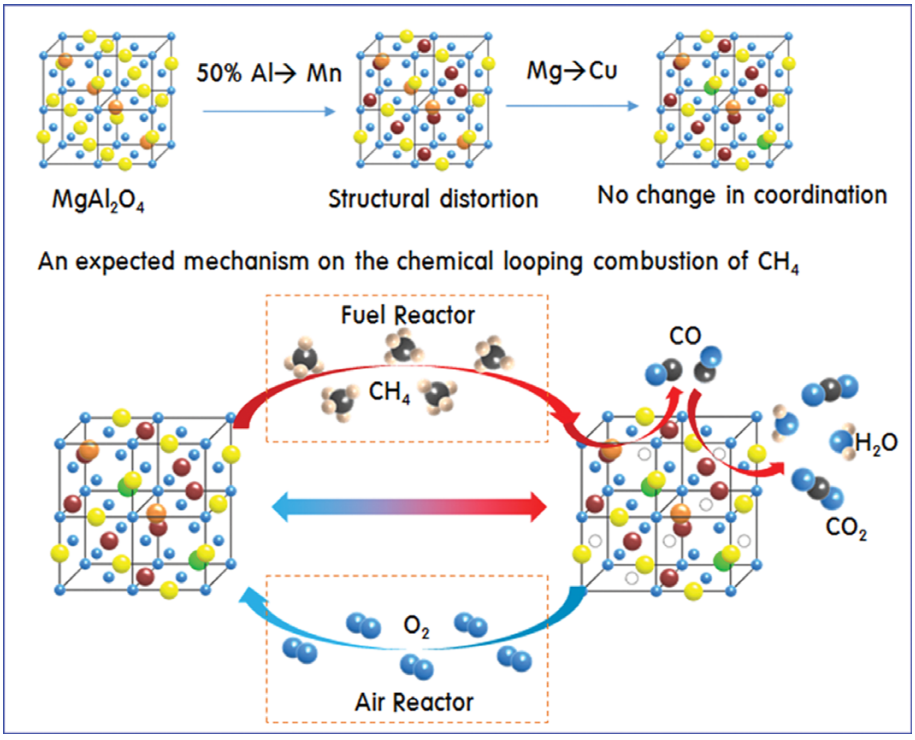

Scheme 2. An expected mechanism for CLC on an spinel $Cu_{0.75}Mg_{0.25}MnAlO_4$.

Cu^{2+}-O lattice of $Cu_{0.75}Mg_{0.25}MnAlO_4$ particle and then converted to an oxidized form such as CO by bonding with oxygen in the lattice, and Cu^{2+} and Mn^{3+} are reduced to Cu^0 and Mn^{2+}. As they receive oxygen from the Al-O and Mg-O lattices and are again oxidized to CuO (partially Cu_2O), the oxygen defects would have resulted from Al-O and Mg-O. The evidence is the Al-OH and Mg-OH curves seen in the Al_{2p} and Mg_{2p} spectra in the XPS results. As a result, the combustion reaction of CH_4 can be expected to be promoted by the oxygen deficiency caused by withdrawing oxygen from the lattice of oxygen carrier particles. Evidence of this conjecture was also seen in the O1s curve. The O1s binding energy curves were seen at 530.3 eV for fresh sample, 530.0 eV for reduced sample, and 530.3 eV for re-oxidized sample, and the areas were similar. However, in the reduced sample, an O_{1s} binding energy curve corresponding to M-OH was observed at 531.2 eV, which can be explained in the same way as the Al-OH and Mg-OH curves mentioned above.

From the XRD and XPS results, the oxygen transfer mechanism in the CLC system could be expected as in Scheme 2. The CH_4 molecules are adsorbed on the surface of the Cu-O-metal of the oxygen carrier particles, and the oxygen is removed from the lattice to be converted to CO and H_2. The oxygen vacancies in the first-stage oxidation reaction ($CH_4 \rightarrow CO$) occur around Cu and form Cu-vacancy-metal (partially Mn-vacancy-metal). At this time, oxygen transfer to Cu (partially Mn) reduced through the adjacent Al-O or Mg-O lattice takes place instantaneously, and oxygen defects eventually migrate to Al and Mg, and Al-vacancy-metal or Mg-vacancy-metal is formed. In the second-stage oxidation reaction ($CO \rightarrow CO_2$), the CO molecules are adsorbed on the regenerated Cu-O-metal (partially Mn-O-metal) surface and then completely oxidized to CO_2, resulting in oxygen defects such as Cu-vacancy-metal (partially Mn-vacancy-metal) in the lattice. This oxygen vacancy is again filled by the oxygen movement of the Al-O-metal or Mg-O-metal lattices, and the redox reaction is continued. Finally, the Al-vacancy-metal or Mg-vacancy-metal lattices with oxygen defects in the fuel reactor is transferred to the air reactor and replenished with oxygen. This cycle is repeated continuously. However, we should not forget the conclusions of CO- and CH_4-TPD analysis. The effect of Mn^{3+} on oxygen transport is not large compared to Cu^{2+}. Furthermore, the substitution of Mn^{3+} in this study does not induce the distortion of the spinel crystal structure compared to the Cu^{2+} substitution. As a result, the bond strength between Mn-O is large and oxygen deficiency is hard to occur. However, in the case of Cu^{2+}, the electron rearrangement of $3d^9$ is likely to cause rearrangement of crystals by Jahn-Teller distortion. Therefore, it is considered that oxygen deficiency easily occurs in the crystal lattice.

CONCLUSIONS

The aim was to improve the oxygen transfer performance by adding Cu_{2+} with good reducing ability to the $MgMnAlO_4$ spinel structure. Even though 75% of the Mg sites were replaced with Cu, the spinel crystals formed were very stable and their crystal structure did not change after repeated redox reactions. In the results of CH_4-TPD, the increase of adsorption amount of CH_4 with increase of Cu amount seems to be more favorable to Cu than other metals. The oxygen transport capacity in the redox reaction increased with the amount of Cu, which meant that the reduction of Cu ultimately influenced the oxygen transfer capacity of the particles. Furthermore, we confirmed from the XPS results that the Al-O and Mg-O lattices in the $MgMnAlO_4$ spinel crystal used as the support can sustain the reaction by transferring oxygen through the lattice to the oxygen-deficient Cu during the redox reaction. Especially, the highest oxygen transfer capacity of $Cu_{0.75}Mg_{0.25}MnAlO_4$ particle was obtained at 7.62%, but it was confirmed that Cu, which was partially crystallized from the XRD results, was not regenerated. Ultimately, the optimum amount of Cu that could be substituted was between 0.5 and 0.75 moles.

ACKNOWLEDGEMENTS

This work was supported by the Energy Efficiency & Resources Programs of the Korea Institute of Energy Technology Evaluation and Planning (KETEP), granted financial resources from the Ministry of Trade, Industry & Energy, Republic of Korea (20152010201840).

REFERENCES

1. S. Sun, L. Wang, X. Liu, B. Jin and D. Wang, *Processes*, **6**, 1 (2018).
2. X. Cheng, K. Li, H. Wang, X. Zhu, Y. Wei, Z. Li, M. Zheng and D. Tian, *Chem. Eng. J.*, **328**, 382 (2017).
3. K. Marx, O. Bertsch, T. Pröll and H. Hofbauer, *Energy Procedia*, **37**, 635 (2013).
4. R. Villa, C. Cristiani, G. Groppi, L. Lietti, P. Forzatti, U. Cornaro and S. Rossini, *J. Mol. Catal. A-Chem.*, **204**, 637 (2003).
5. M. M. Hossain and H. I. Lasa, *AIChE. J.*, **53**, 1817 (2007).
6. S. Kang, Y. Im, K. S. Park, T. W. Cho, J. Jeon, K. I. Chung and M. Kang, *Electrochim. Acta*, **209**, 623 (2016).
7. B. S. Kwak, N. K. Park, J. I. Baek, H. J. Ryu and M. Kang, *Korean J. Chem. Eng.*, **37**, 1936 (2017).
8. B. S. Kwak, N. K. Park, H. J. Ryu, J. I. Baek and M. Kang, *Appl. Therm. Eng.*, **128**, 1273 (2018).
9. C. Linderholm, A. Abad, T. Mattisson and A. Lyngfelt, *Int. J. Greenh. Gas Con.*, **2**, 520 (2008).
10. A. R. Puigdollers, P. Schlexer, S. Tosoni and G. Pacchioni, *ACS Catal.*, **7**, 6493 (2017).
11. B. S. Kwak, N. K. Park, S. O. Ryu, J. I. Baek, H. J. Ryu and M. Kang, *Chem. Eng. J.*, **309**, 617 (2017).
12. N. Son, J. Y. Do, N. K. Park, S. O. Ryu, B. S. Kwak, J. I. Baek, U. S. Kim, H. J. Ryu, D. Lee and M. Kang, *Int. J. Energy Res.*, **42**, 3943 (2018).
13. J. Y. Do, J. H. Lee, N. K. Park, T. J. Lee, S. T. Lee and M. Kang, *Chem. Eng. J.*, **334**, 1668 (2018).
14. J. Y. Do, N. Son, N. K. Park, B. S. Kwak, J. I. Baek, H. J. Ryu and M. Kang, *Appl. Energy*, **219**, 138 (2018).
15. H. J. Ryu, S. Y. Lee, Y. C. Park and M. H. Park, *World Acad. Sci. Eng. Technol.*, **28**, 169 (2007).
16. Y. Zhu, X. Liu, S. Jin, H. Chen, W. Lee, M. Liu and Y. Chen, *J. Mater. Chem. A.*, **7**, 5875 (2019).
17. K. Singh, F. Razmiooei and J. S. Yu, *J. Mater. Chem. A*, **5**, 20095 (2017).
18. N. A. Gribchenkova, K. G. Snorchkov, A. G. Kolmakov and A. S.

Alikhanyan, *Inorg. Mater.*, **54**, 575 (2018).
19. K. Rajar Soomro, Z. H. Ibupoto and B. Sirajuddin, *Int. J. Food Prop.*, **20**, 1359 (2017).
20. L. Schreyeck, A. Wlosik and H. Fuzellier, *J. Mater. Chem.*, **11**, 483 (2001).
21. F. G. Labiano, L. F. Diego, J. Adánez, A. Abad and P. Gayán, *Chem. Eng. Sci.*, **60**, 851 (2005).
22. M. Kogler, E. M. Köck, T. Bielz, K. Pfaller, B. Klötzer, D. Schmidmair, L. Perfler and S. Penner, *J. Phys. Chem. C.*, **118**, 8435 (2014).
23. Z. Sihaib, F. Puleo, G. Pantaleo, V. L. Parola, J. L. Valverde, S. Gil, L. F. Liotta and A. Giroir-Fendler, *Catalysts*, **9**, 226 (2019).
24. L. Qiu, Y. Wang, D. Pang, F. Ouyang, C. Zhang and G. Cao, *Catalysts*, **6**, 9 (2016).
25. C. Huo, J. Ouyang and H. Yang, *Sci. Rep.*, **4**, 3682 (2014).
26. W. Qin, C. Lin, J. Wang, X. Xiao, C. Dong and L. Wei, *Energies*, **9**, 1 (2016).
27. K. M. Kim, B. S. Kwak, N. K. Park, T. J. Lee, S. T. Lee and M. Kang, *J. Ind. Eng. Chem.*, **46**, 324 (2017).
28. I. Qian and Z. Yan, *J. Nat. Gas Chem.*, **11**, 151 (2002).
29. S. Sun, D. Mao, J. Yu, Z. Yang, G. Lu and Z. Ma, *Catal. Sci. Technol.*, **5**, 3166 (2015).
30. J. R. Scheffe, A. H. McDaniel, M. D. Allendorf and A. W. Weimer, *Energy Environ. Sci.*, **6**, 963 (2013).
31. J. Adánez, L. de Diego, F. García-Labiano, P. Gayán, A. Abad and J. M. Palacios, *Energy Fuels*, **18**, 371 (2004).
32. P. Cho, T. Mattisson and A. Lyngfelt, *Fuel*, **83**, 1215 (2004).
33. J. G. Wang, C. Zhang, D. Jin, K. Xie and B. Wei, *J. Mater. Chem. A.*, **3**, 13699 (2015).
34. P. H. Zhou, L. J. Deng, J. L. Xie, D. F. Liang, L. Chen and X. Q. Zhao, *J. Magn. Magn. Mater.*, **292**, 325 (2005).
35. F. G. Labiano, L. F. Diego, J. Adánez, A. Abad and P. Gayán, *Chem. Eng. Sci.*, **60**, 851 (2005).
36. S. Poulston, P. M. Parlett, P. Stone and M. Bowker, *Surf. Interface Anal.*, **24**, 811 (1996).
37. J. P. Espinós, J. Morales, A. Barranco, A. Caballero, J. P. Holgado and A. R. González-Elipe, *J. Phys. Chem. B.*, **106**, 6921 (2002).
38. J. Y. Zhang, Z. L. Wu, S. G. Wang, C. J. Zhao and G. Yang, *Appl. Phys. Lett.*, **102**, 102404 (2013).
39. Y. Luo, X. Wang, W. Guo and M. Rohwerder, *J. Electrochem. Soc.*, **162**, 294 (2015).
40. X. Li, M. Xin, S. Guo, T. Cai, D. Du, W. Xing, L. Zhao, W. Guo, Q. Xue and Z. Yan, *Electrochim. Acta*, **253**, 302 (2017).
41. E. Ksepko, P. Badinski and L. Nalbandian, *Appl. Energy*, **190**, 1258 (2017).
42. J. Gan, X. Lu, J. Wu, S. Xie, T. Zhai, M. Yu, Z. Zhang, Y. Mao, S. C. I. Wang, Y. Shen and Y. Tong, *Sci. Rep.*, **3**, 1021 (2013).